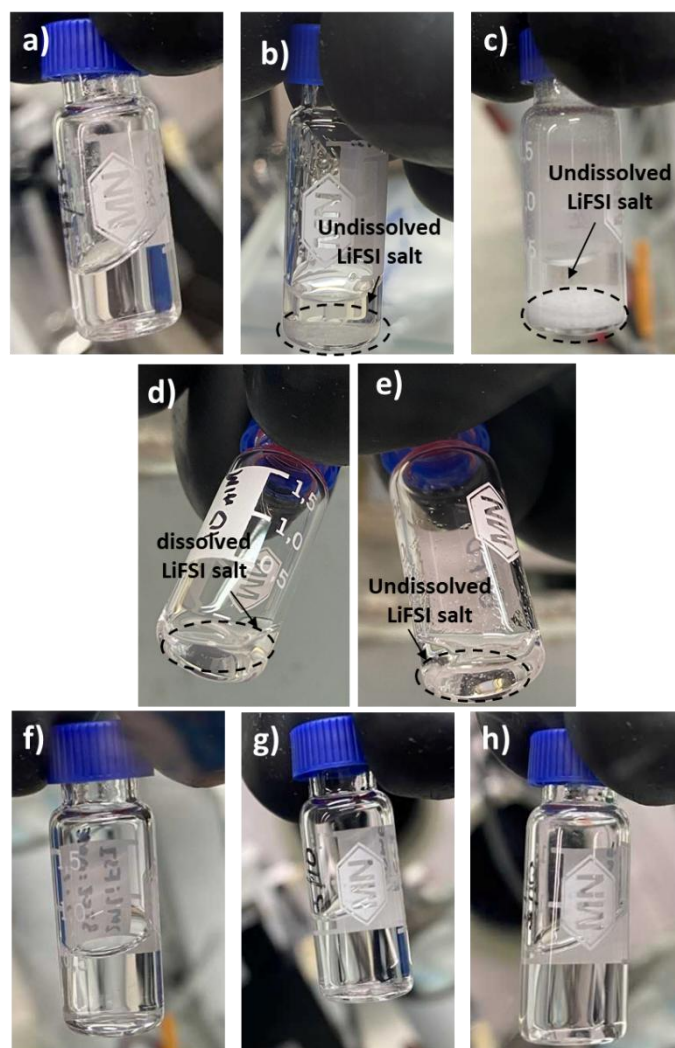


## 97.SUPPORTING INFORMATION

### Enhanced Performance of Lithium Metal Batteries via Cyclic Fluorinated Ether Based Electrolytes

#### Note 1: Electrolyte solvent composition choice

As LiFSI showed very poor solubility (**Fig. S1 b and c**) in both the BTFE (solubility 10– 100 mM, **Fig. S1d**) and BTFD fluorinated solvents (solubility <10 mM, **Fig. S1e**), DME was added as a co-solvent (**Fig. S1 f-h**). The solvent vs. co-solvent ratio was optimized by observing the efficiency of the Li stripping and plating in Li|Cu cells (**Fig. S2**) and benchmarked vs. using 1 M LiFSI in DME, which resulted in short circuits by the 25<sup>th</sup> cycle. A BTFD:DME ratio of 1:3 (v:v) increased the stability, with the cells operating until approx. the 75<sup>th</sup> cycle, and they operated until the 500<sup>th</sup> cycle using a BTFD:DME ratio of 1:1 (v:v). A BTFD:DME ratio of 3:1 (v:v) reduced the cycle-life to the 200<sup>th</sup> cycle. The overpotential increased as a function of BTFD:DME ratio. Looking at the densities, viscosities, and ionic conductivities for the different BTFD:DME ratios, the two former increase with the BTFD content, but the latter decreases (**Fig. S3**). Henceforth, the intermediate 1:1 (v:v) ratio was chosen as the optimal electrolyte solvent composition, rendering four electrolytes: 1 M LiFSI in DME (as reference), 1 M LiFSI in BTFE:DME 1:1 (v:v), 1 M LiFSI in BTFD:DME 1:1 (v:v), and 2 M LiFSI in BTFD:DME 1:1 (v:v). We only state the salt concentration and the solvents used from here forth.



**Fig. S1.** Photographs of different electrolytes: (a) 1 M LiFSI in DME, (b) 1 M LiFSI in BTFE, (c) 1 M LiFSI in BTFD, (d) dissolved LiFSI salt in BTFE with 10 mM LiFSI concentration, (e) undissolved LiFSI salt in BTFD with 10 mM LiFSI concentration (f) 1 M LiFSI in BTFE:DME (1:1, v:v), (g) 1 M LiFSI in BTFD:DME (1:1, v:v), and (h) 2 M LiFSI in BTFE:DME (1:1, v:v).

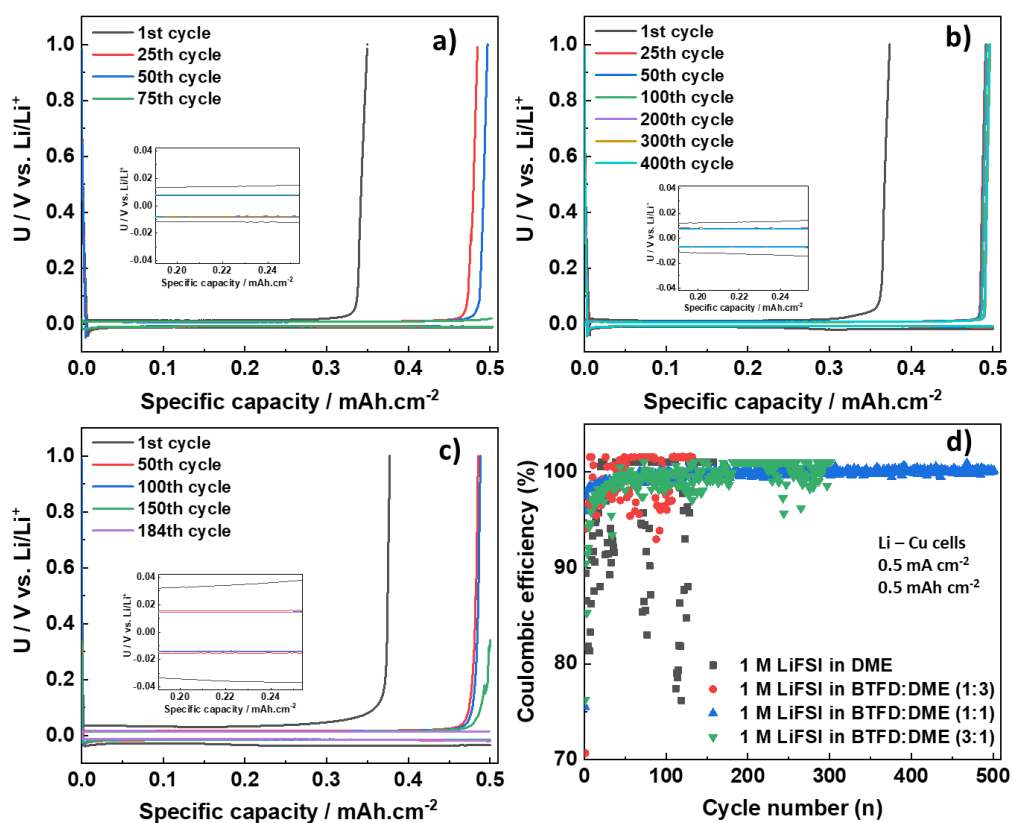


**Fig. S2.** Li stripping and plating profiles of Li|Cu half-cells tested at a current density of 0.5 mA cm<sup>-2</sup> with a cutoff capacity of 0.5 mAh cm<sup>-2</sup> using: (a) 1 M LiFSI in BTFD:DME (1:3, v:v), (b) 1 M LiFSI in BTFD:DME (1:1, v:v), (c) 1 M LiFSI in BTFD:DME (3:1, v:v) electrolytes, and (d) CEs for the same cells, conditions and electrolytes (and 1 M LiFSI in DME as reference).

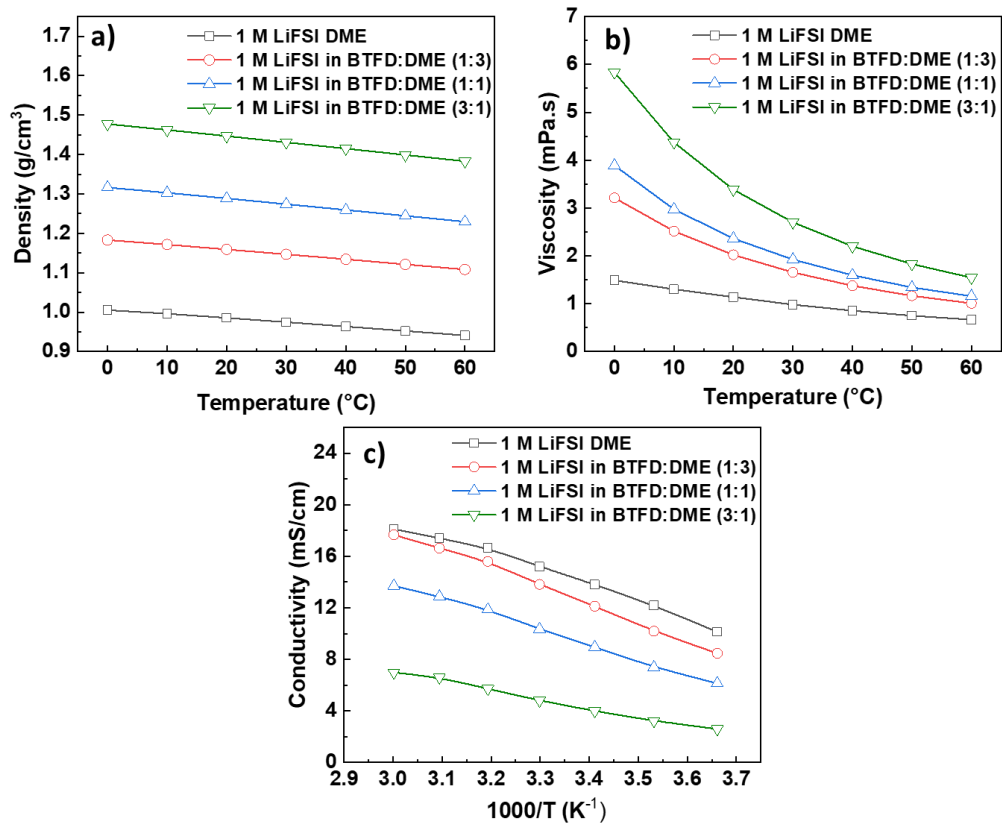


**Fig. S3.** Physicochemical properties as functions of temperature for the different electrolytes: (a) density, (b) viscosity, and (c) ionic conductivity.

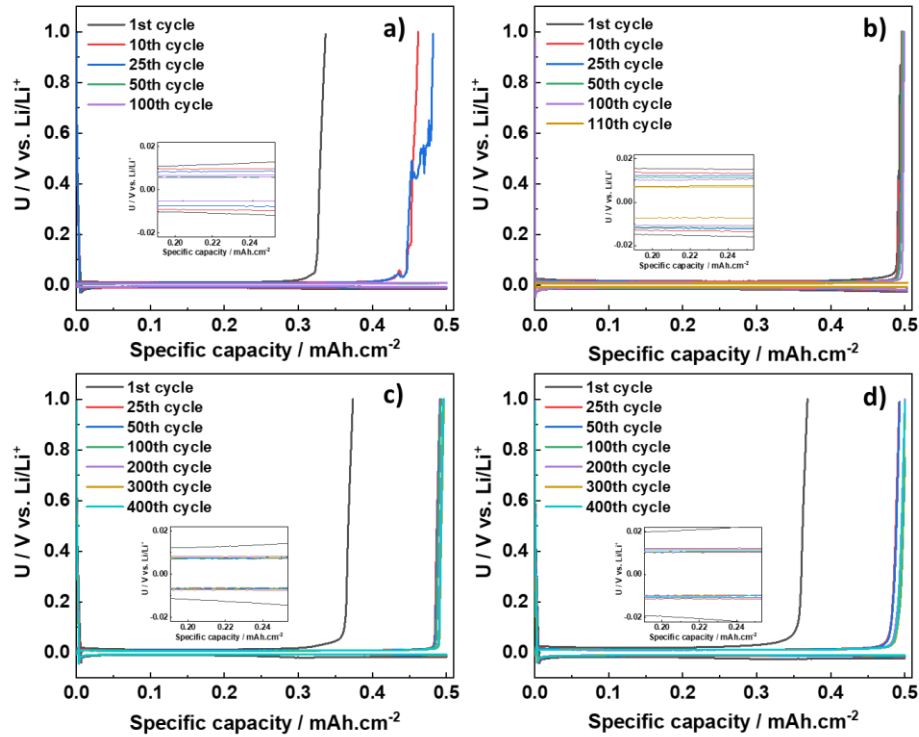


**Fig. S4.** Li stripping and plating profiles of Li|Cu half-cells tested at a current density of  $0.5 \text{ mA cm}^{-2}$  with a cutoff capacity of  $0.5 \text{ mAh cm}^{-2}$  using: (a) 1 M LiFSI:DME, (b) 1 M LiFSI in BTFE:DME, (c) 1 M LiFSI in BTFD:DME, and (d) 2 M LiFSI in BTFD:DME electrolytes.

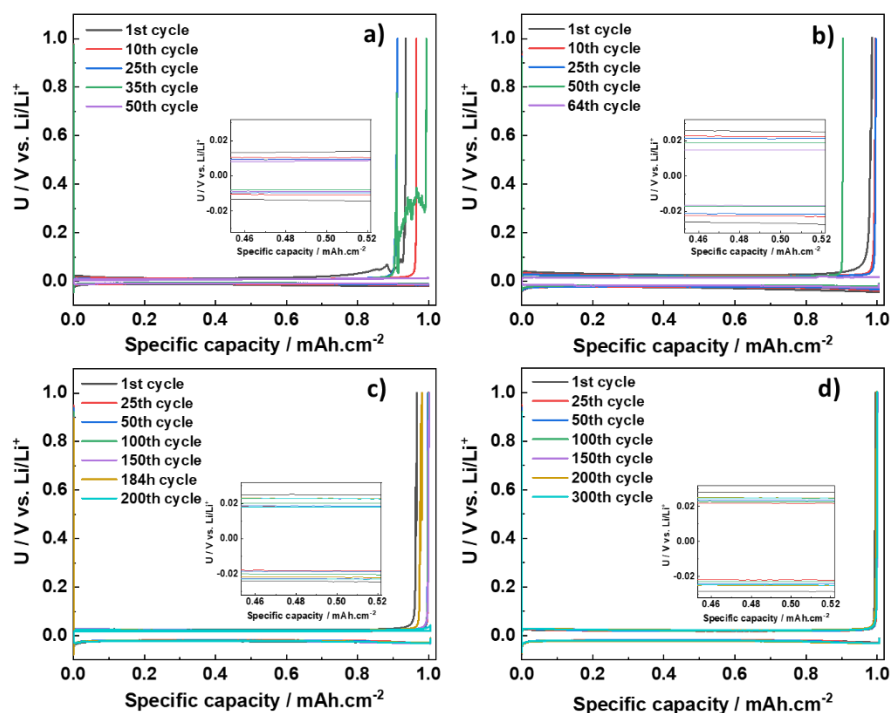


**Fig. S5.** Li stripping and plating profiles of Li|Cu half-cells tested at a current density of  $1.0 \text{ mA cm}^{-2}$  with a cutoff capacity of  $1.0 \text{ mAh cm}^{-2}$  using: (a) 1 M LiFSI:DME, (b) 1 M LiFSI in BTFE:DME, (c) 1 M LiFSI in BTFD:DME, and (d) 2 M LiFSI in BTFD:DME electrolytes.

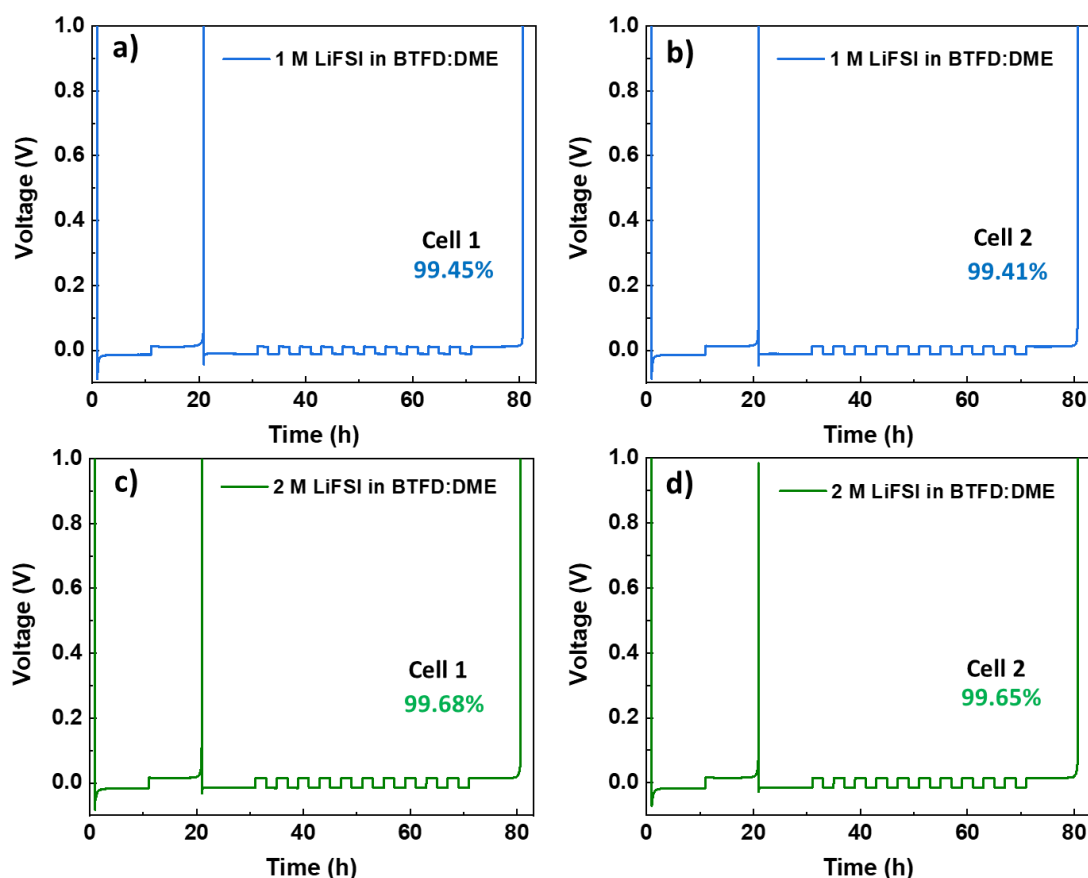


**Fig. S6.** Reproducibility tests of average CE applying the Aurbach method [1] on Li | Cu half-cells using: (a,b) 1 M LiFSI in BTFD:DME and (c,d) 2 M LiFSI in BTFD:DME electrolytes.

**Table S1.** CEs and cycle life data for different electrolytes in Li | Cu half-cells.

	Testing conditions	1 M LiFSI in DME	1 M LiFSI in BTFE:DME	1 M LiFSI in BTFD:DME	2 M LiFSI in BTFD:DME
CE (%)	0.5 mA cm <sup>-2</sup> to 0.5 mAh cm <sup>-2</sup>	99.8	99.3	99.4	99.6
	1.0 mA cm <sup>-2</sup> to 1.0 mAh cm <sup>-2</sup>	98.2	99.2	99.4	99.6
Cycle life (number of cycles)	0.5 mA cm <sup>-2</sup> to 0.5 mAh cm <sup>-2</sup>	35	75	400	400
	1.0 mA cm <sup>-2</sup> to 1.0 mAh cm <sup>-2</sup>	20	50	180	280
CE (%) by Aurbach method	[1]	97.8	99.3	99.4	99.6

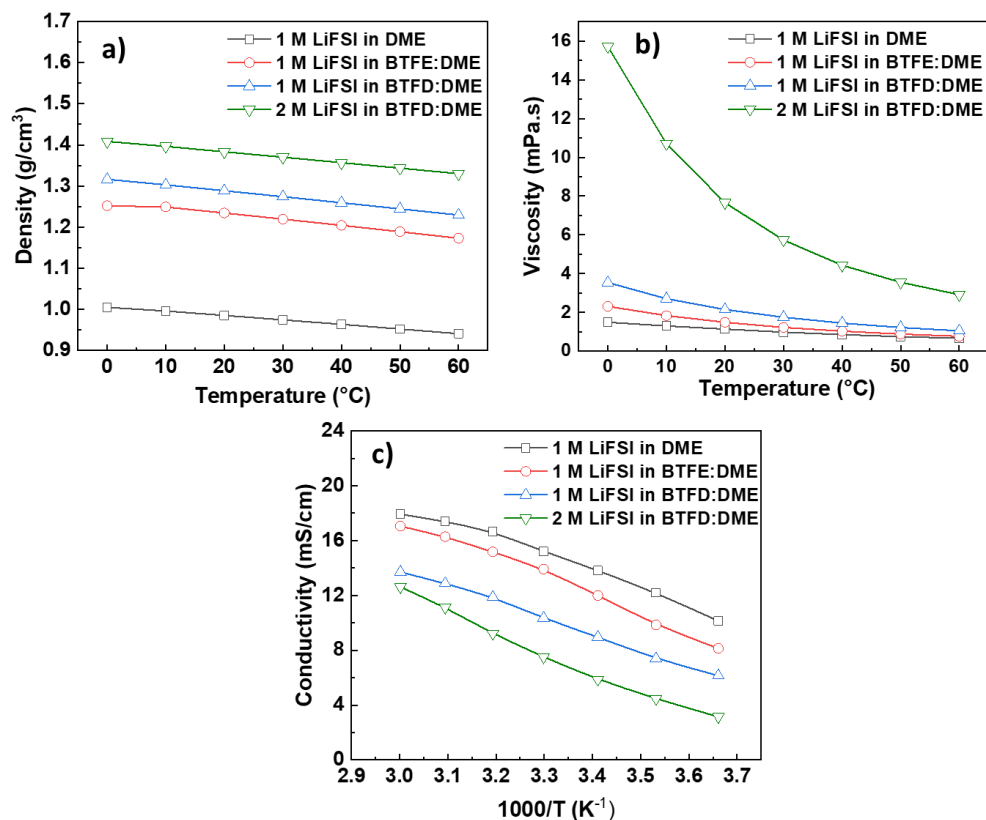


**Fig. S7.** Physicochemical properties as functions of temperature for the different electrolytes: (a) density, (b) viscosity, and (c) ionic conductivity.

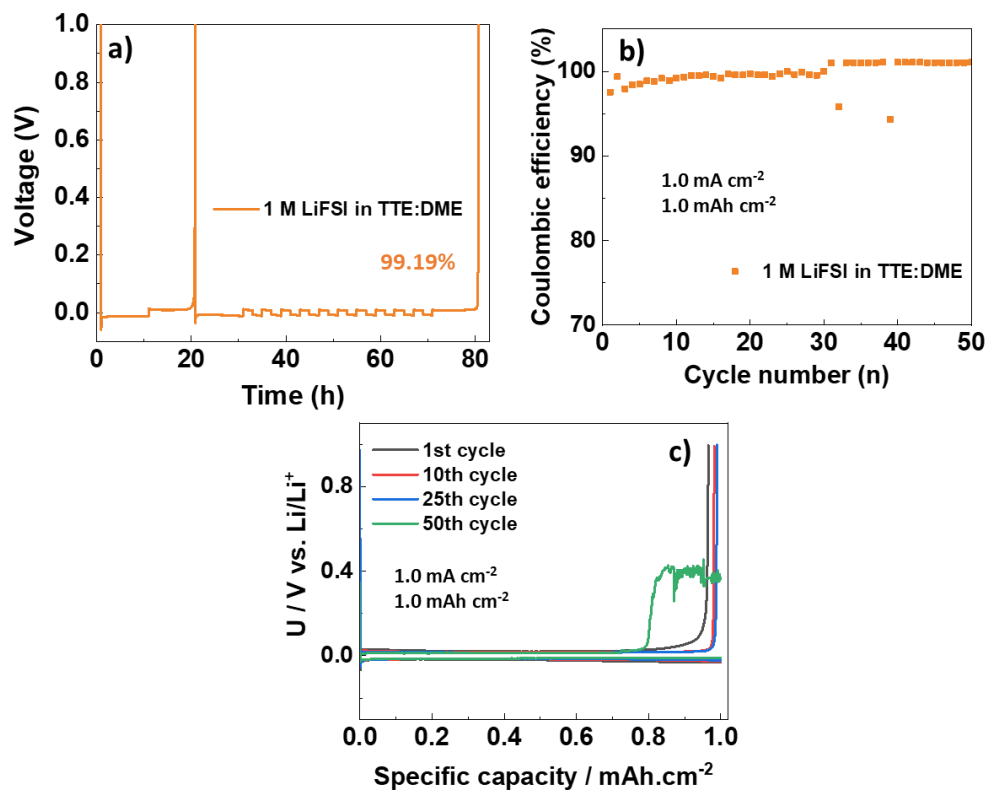


**Fig. S8.** CE of Li plating and stripping of Li | Cu cells using 1 M LiFSI in TTE:DME electrolyte from (a) the standard Aurbach method (b) galvanostatic cycling. (c) Li plating and stripping profiles of Li | Cu half-cells tested at a current density of  $1.0 \text{ mA cm}^{-2}$  with a cutoff capacity of  $1.0 \text{ mAh cm}^{-2}$ .

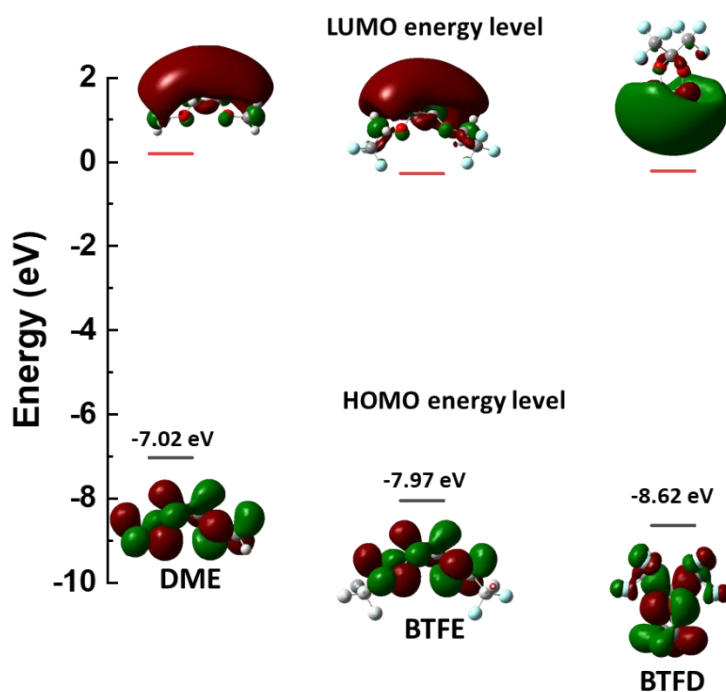


**Fig. S9.** HOMO-LUMO energy levels of different solvents as calculated by DFT (B3LYP/6-311++G\*\*) using Gaussian 09 [2].



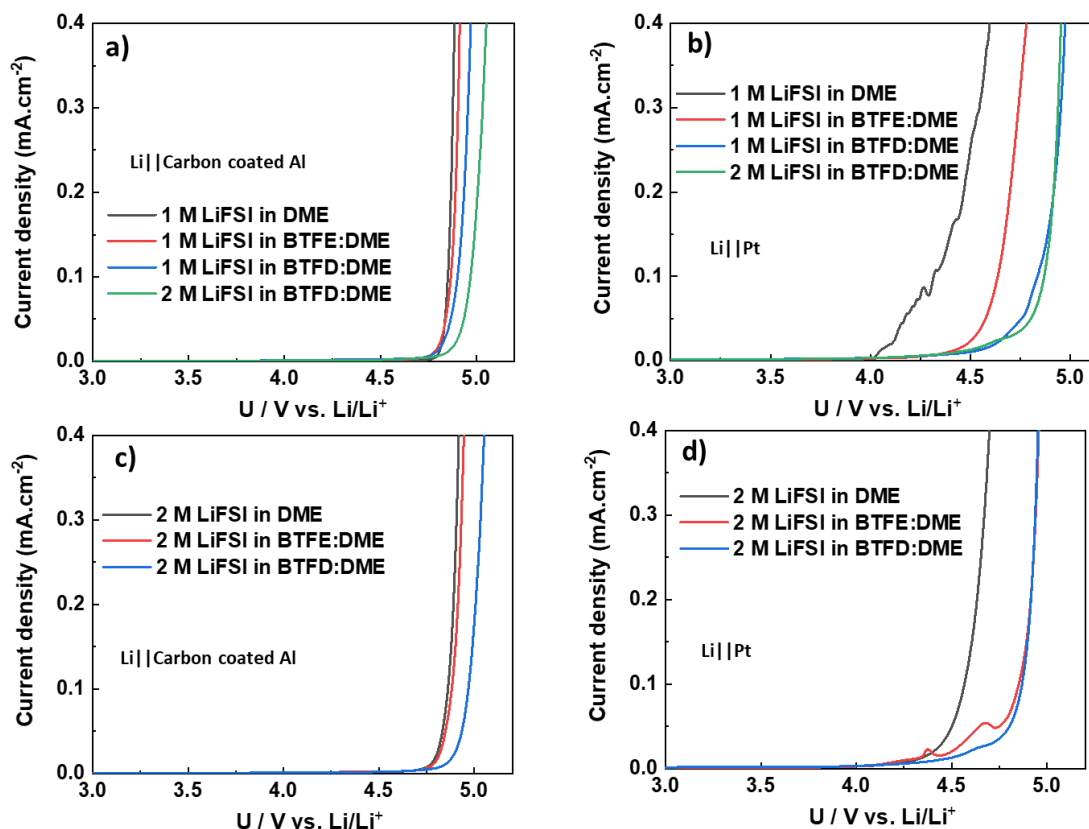


**Fig. S10.** Oxidative LSV for the tested electrolytes measured in (a) Li || carbon-coated Al cells and (b) Li || Pt cells. Oxidative LSV for different electrolytes with 2 M concentrations measured in (c) Li || carbon-coated Al cells and (d) Li || Pt cells.

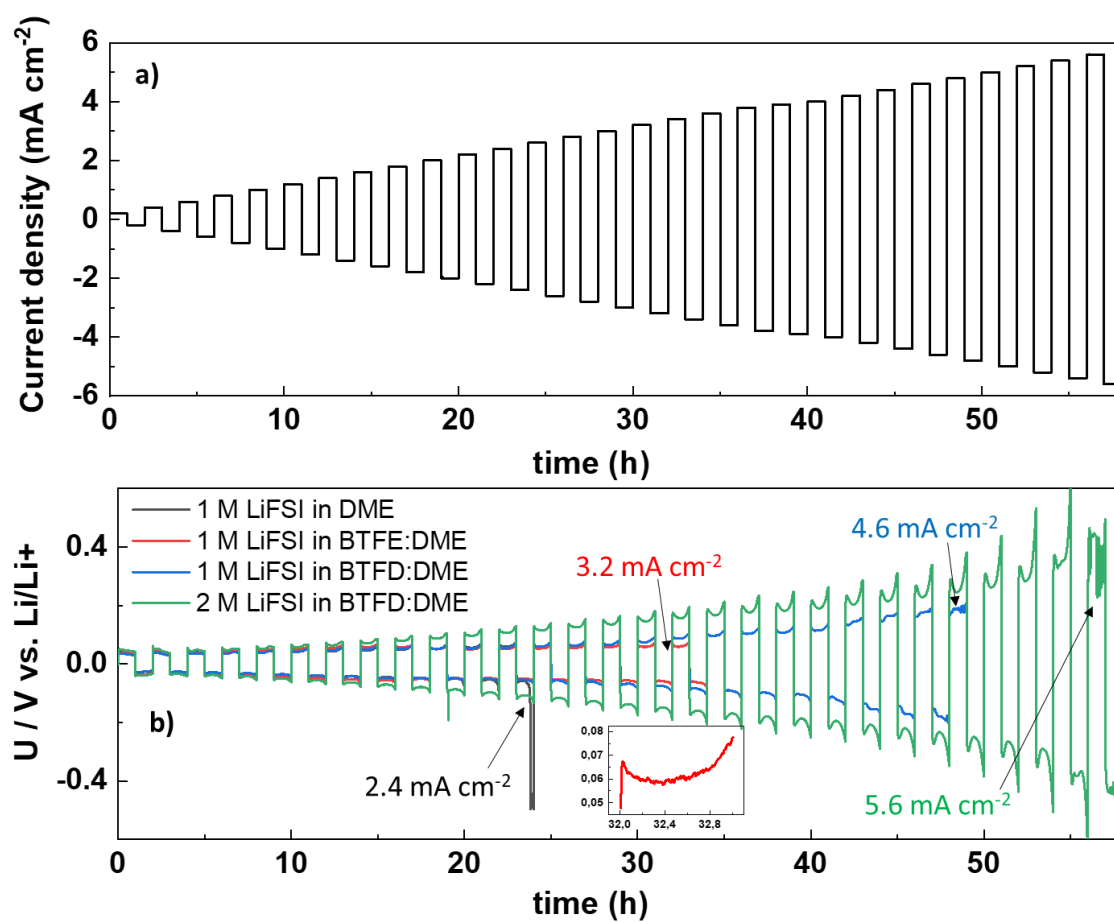


**Fig. S11.** CCD tests done on Li||Li cells using different electrolytes: (a) the time-control protocol used for CCD and (b) Li plating and stripping overpotentials and CCDs for different electrolytes.

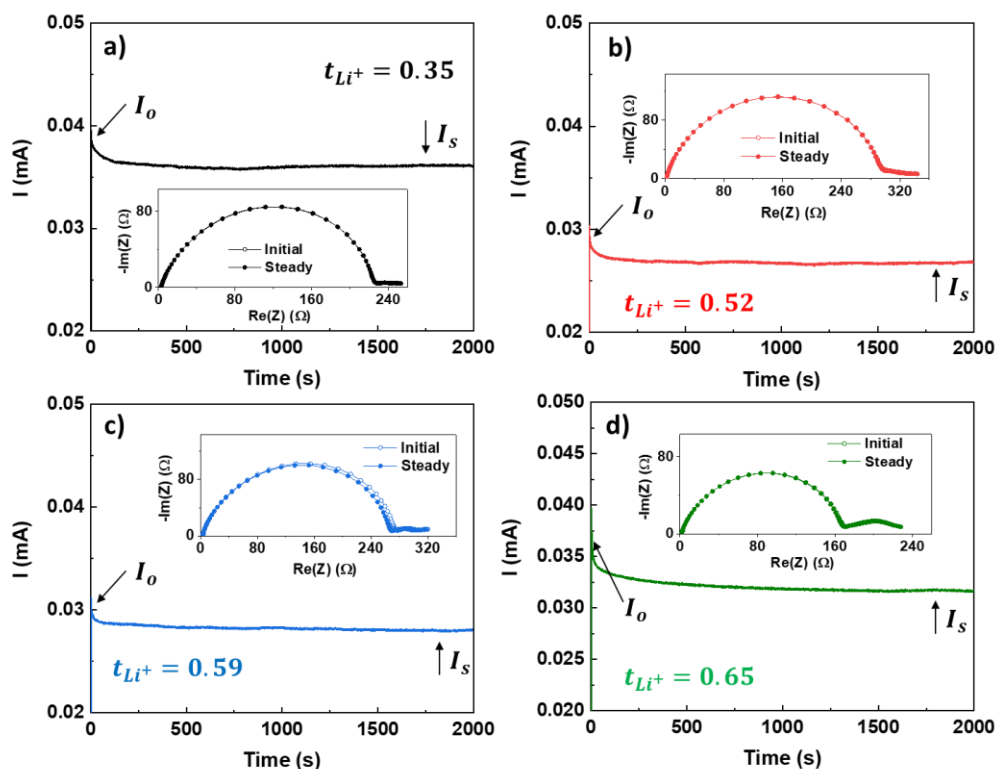


**Fig. S12.**  $\text{Li}^+$  transport numbers and chronoamperometry profiles of  $\text{Li}||\text{Li}$  symmetrical cells using: (a) 1 M LiFSI in DME, (b) 1 M LiFSI in BTFE:DME, (c) 1 M LiFSI in BTFD:DME, and (d) 2 M LiFSI in BTFD:DME electrolytes under a DC polarization of 10 mV.

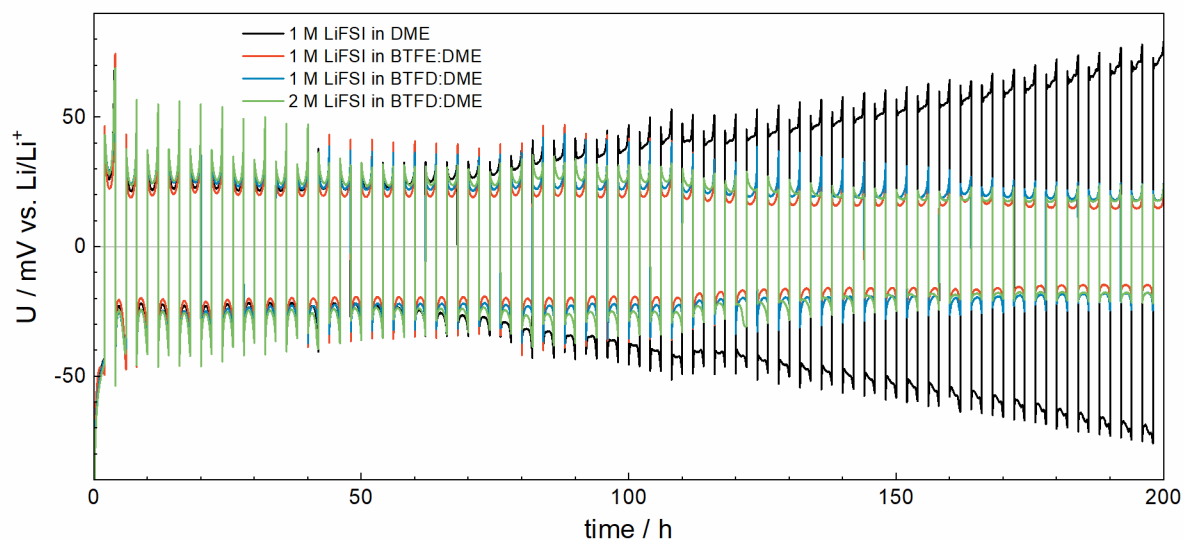


**Fig. S13.**  $\text{Li}||\text{Li}$  symmetric cells cycled at a current density of  $0.5 \text{ mA cm}^{-2}$  to a cutoff capacity of  $1.0 \text{ mAh cm}^{-2}$  using the different electrolytes.

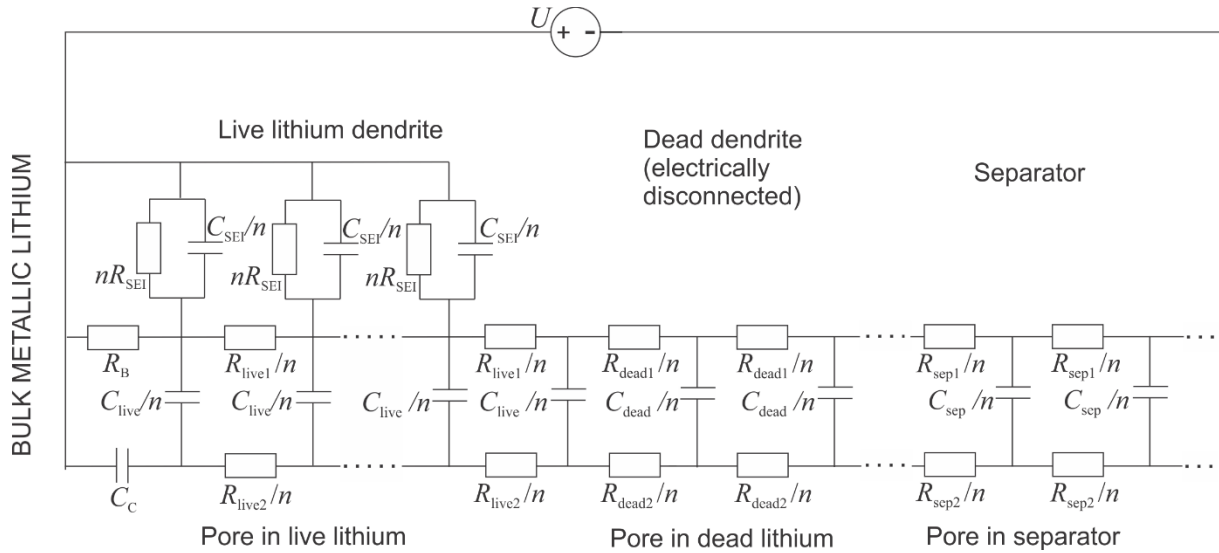


**Fig. S14.** Transmission line model equivalent circuit used to simulate the cycled Li||Li symmetric cell spectra.

In the model of the cell, three different porous layers are considered. From the right to the left in **Fig. S14**: the porous separator, the completely passivated (“dead”) high surface area lithium layer, and the high surface area “live” lithium layer. The transport of both the active ion ( $\text{Li}^+$ , upper rail, elements with index 1) and the inactive ions (lower rail, elements with index 2) through the layers are considered. These rails end on the left side with elements describing the interaction of the corresponding ions with the electrode.

The completely passivated “dead” lithium is considered to act as another porous separator layer. The “dead” lithium is made of the components of the SEI and disconnected Li metal formed through the following two processes: i) Li metal in high surface area deposits is readily passivated, forming an SEI shell on its surface. This shell remains on the electrode after Li metal is stripped from it. Through cycling, this remaining SEI accumulates, since more of it is produced every cycle of plating and stripping. Its thickness, porosity and tortuosity are dependent on the morphology of the high surface area lithium deposits and the SEI formation; ii) Some of the deposited Li metal can become electronically disconnected, which means that it cannot be recovered in subsequent stripping. This means it is possible that some Li metal fragments disconnected from the bulk Li metal electrode remain inside the previously mentioned SEI shell. The live lithium dendrite layer on the other hand describes the interaction of the active and non-active ions with the high surface area Li, which is still electronically connected with the bulk Li metal electrode. This configuration essentially means that the electrode is porous, not flat.

For the non-cycled Li metal electrode, the TLM circuit is simpler, since only the SEI components and the separator need to be considered (**Fig. S15**). The model again includes the transport of both the active ion ( $\text{Li}^+$ , upper rail, elements with index 1) and the inactive ions (lower rail, elements with index 2) through the layers. Diffusional transport can take place through both the porous separator and the porous SEI. The rails end on the left side with elements describing the interaction of the corresponding ions with the flat electrode. Since only  $\text{Li}^+$  ions can migrate through the compact SEI, the upper rail shows a resistive element (i.e. SEI resistance), while the lower rail, which corresponds to the transport of inactive ions ends with a capacitor.

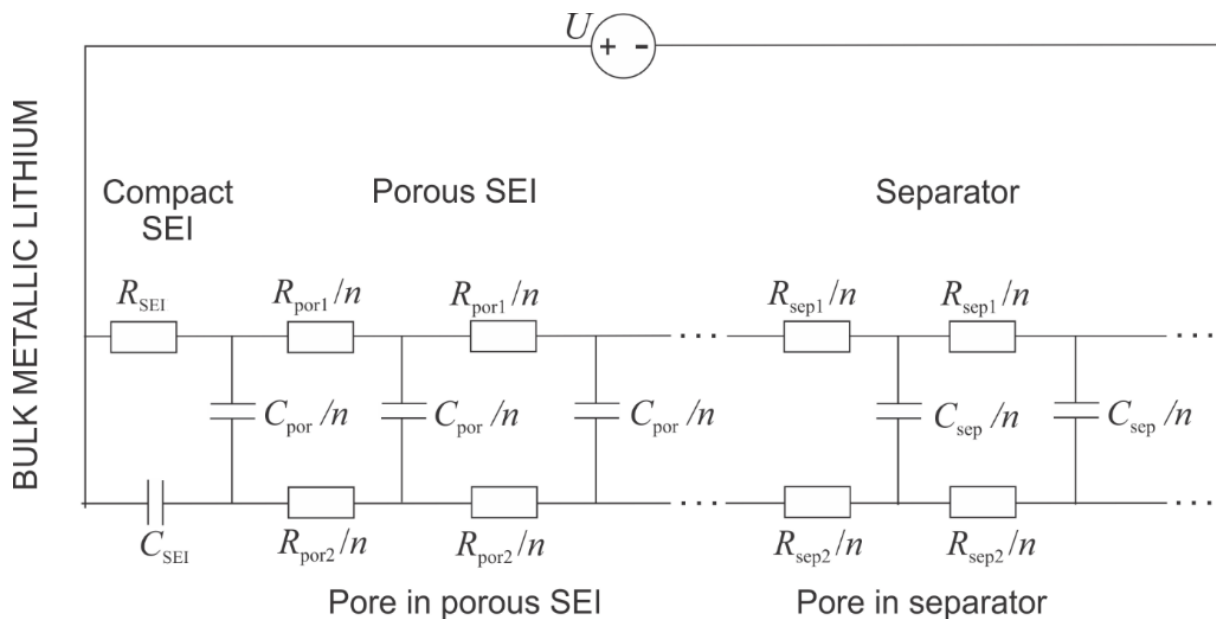


**Fig. S15.** Transmission line model equivalent circuit used to simulate the non-cycled Li || Li symmetric cell spectra.

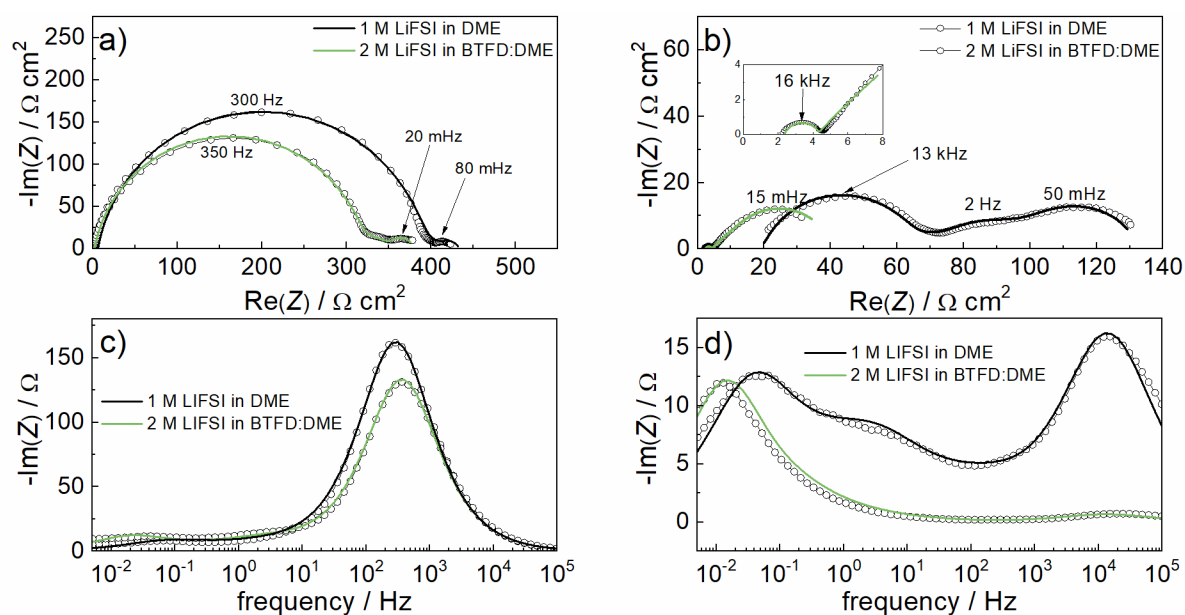


**Fig. S16.** Simulation of: a) non-cycled and b) cycled Li || Li cell spectra from **Fig. 2**. c) and d) shows the same data in Bode plot representation as a) and b), respectively. Measured data = empty circles and the simulations (using the TLMs from **Fig. S14** and **Fig. S15**, respectively) = lines.

**Table S2:** Simulation data from **Fig S16** obtained using the TLMs of **Fig S14** and **Fig S15**, respectively.

	1 M LiFSI in DME non-cycled	1 M LiFSI in DME cycled	2 M LiFSI in BTfD:DME non-cycled	2 M LiFSI in BTfD:DME cycled
$R_{SEI} (\Omega)$	385	47	315	2
$C_{SEI} (s^{\alpha_{SEI}} \Omega^{-1})$	$3.2 \cdot 10^{-6}$	$4 \cdot 10^{-6}$	$3.2 \cdot 10^{-6}$	$1 \cdot 10^{-4}$
$\alpha_{SEI}$	0.89	0.89	0.89	0.89
$R_{por1} (\Omega)$	20		30	
$C_{por} (s^{\alpha_{por}} \Omega^{-1})$	0.01		0.008	
$R_{por2} (\Omega)$	0.5		0.5	
$\alpha_{por}$	0.8		0.8	
$R_{sep1} (\Omega)$	28	28	35	35
$C_{sep} (s^{\alpha_{sep}} \Omega^{-1})$	0.1	0.005	0.35	0.35
$R_{sep2} (\Omega)$	7.5	7.5	2	2
$\alpha_{sep}$	0.75	0.75	0.75	0.85
$R_B$		disregarded		disregarded
$C_C$		disregarded		disregarded
$R_{live1} (\Omega)$		25		2
$C_{live} (s^{\alpha_{live}} \Omega^{-1})$		0.0003		0.03
$R_{live2} (\Omega)$		7.5		0.1
$\alpha_{live}$		0.75		0.75
$R_{dead1} (\Omega)$		50		3
$C_{dead} (s^{\alpha_{dead}} \Omega^{-1})$		0.1		0.001
$R_{dead2} (\Omega)$		15		0.5
$\alpha_{dead}$		0.75		0.75

$C_{dead}$  corresponds to the total chemical capacitance in the dead lithium layer ( $C_{tot}^{chem}$ ), which is dependent on the chemical capacitance of both the active ( $C_1^{chem}$ ) and inactive ions ( $C_2^{chem}$ ) in that layer according to the equations below, where  $A_g$  is the geometric surface area of the electrodes,  $L$  is the thickness of the porous layer in question,  $F$  is Faraday's constant,  $R$  is the gas constant,  $T$  is the temperature,  $n$  is the number of electrons transferred, and  $c$  is the electrolyte salt concentration.

$$C_1^{chem} = \frac{A_g L F^2}{RT} n_1^2 c_1 \quad \text{Eq. 1}$$

$$C_2^{chem} = \frac{A_g L F^2}{RT} n_2^2 c_2 \quad \text{Eq. 2}$$



$$C_{tot}^{chem} = \frac{C_1^{chem} C_2^{chem}}{C_1^{chem} + C_2^{chem}} \quad \text{Eq. 3}$$

Since other parameters are kept constant, the difference between the chemical capacitances of the two electrolytes originates from the difference in the thickness of the dead lithium layer and the concentration of the ions present.  $C_{dead}$  for the 1 M LiFSI in DME electrolyte is 100x larger than for the 2 M LiFSI in BTFD:DME electrolyte. Accounting for the difference in electrolyte salt concentration and the soft short-circuit effect in the 1 M LiFSI in DME electrolyte, the difference could in reality also be larger.

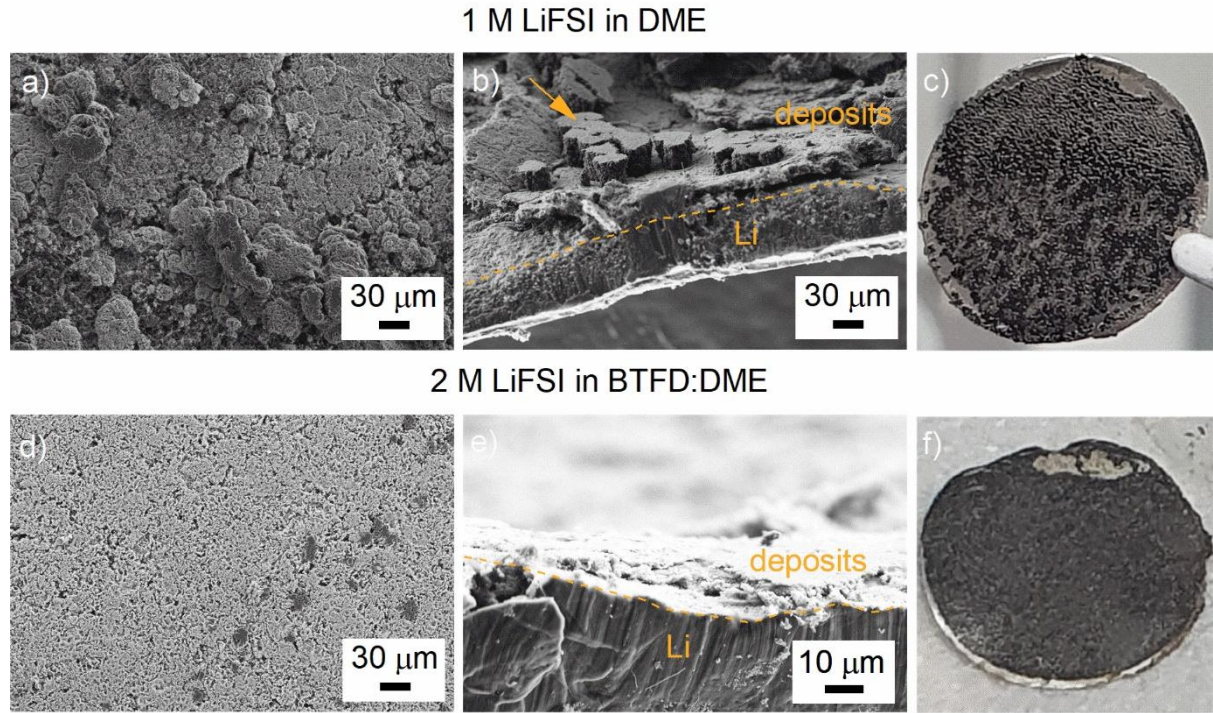


**Fig. S17.** SEM micrographs and photographs of Li metal electrodes extracted from symmetrical Li || Li cells after 50 stripping and plating cycles at  $0.5 \text{ mA cm}^{-2}$  current density (**Fig. S13**) using: (a,b,c) 1 M LiFSI in DME and (d,e,f) 2 M LiFSI in BTFD:DME electrolytes.

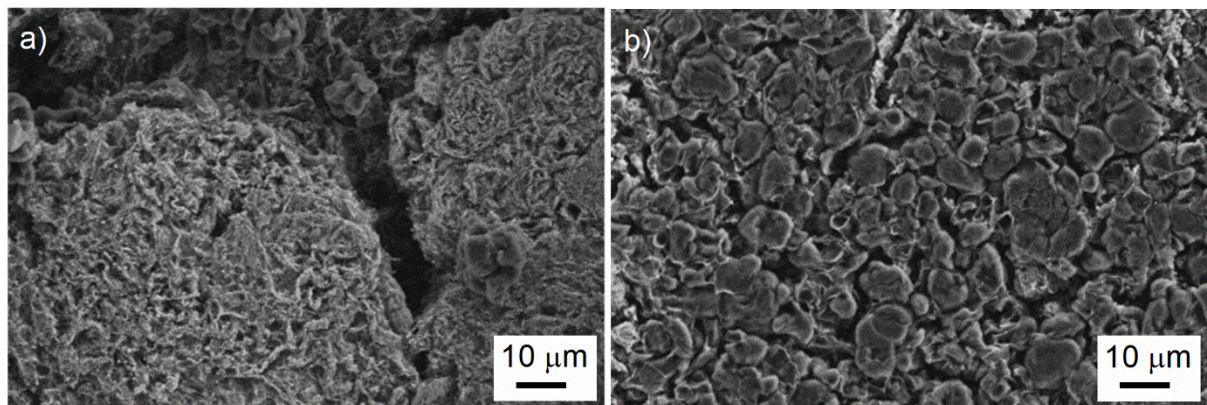


**Figure S18:** SEM micrographs of Li metal electrodes extracted from symmetrical Li || Li cells after 50 plating and stripping cycles at  $0.5 \text{ mA cm}^{-2}$  current density (**Fig. S17**) at higher magnifications: a) 1 M LiFSI in DME and b) 2 M LiFSI in BTFD:DME electrolytes.

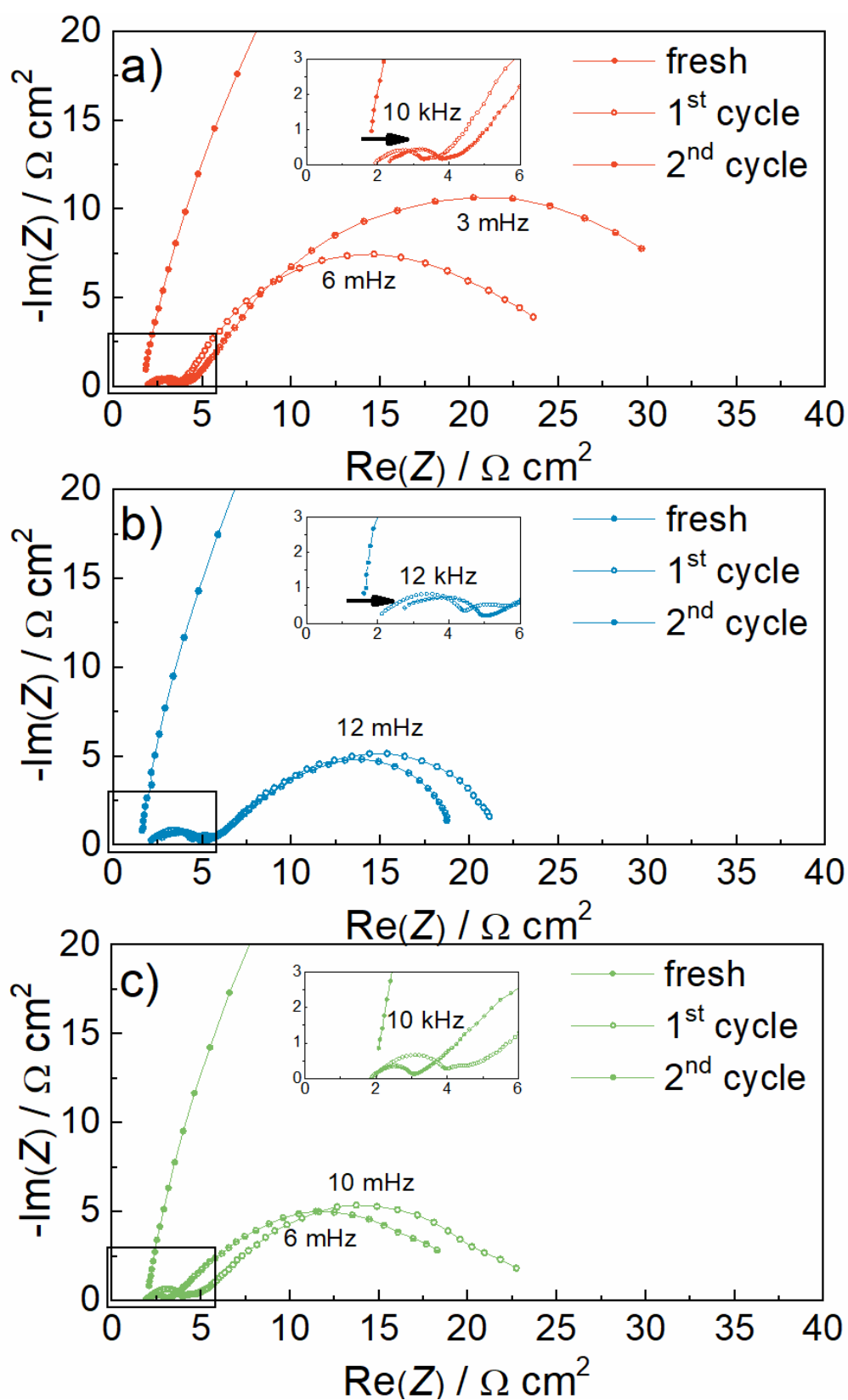


**Figure S19.** Lower magnification impedance spectra for symmetrical Li|Li cells stripped and plated at a current density of  $5 \text{ mA cm}^{-2}$  using: a) 1 M LiFSI in BTFE:DME, b) 1 M LiFSI in BTFD:DME, and c) 2 M LiFSI in BTFD:DME electrolytes. Inserts are shown in the main paper as **Figs. 2e, f and g**.



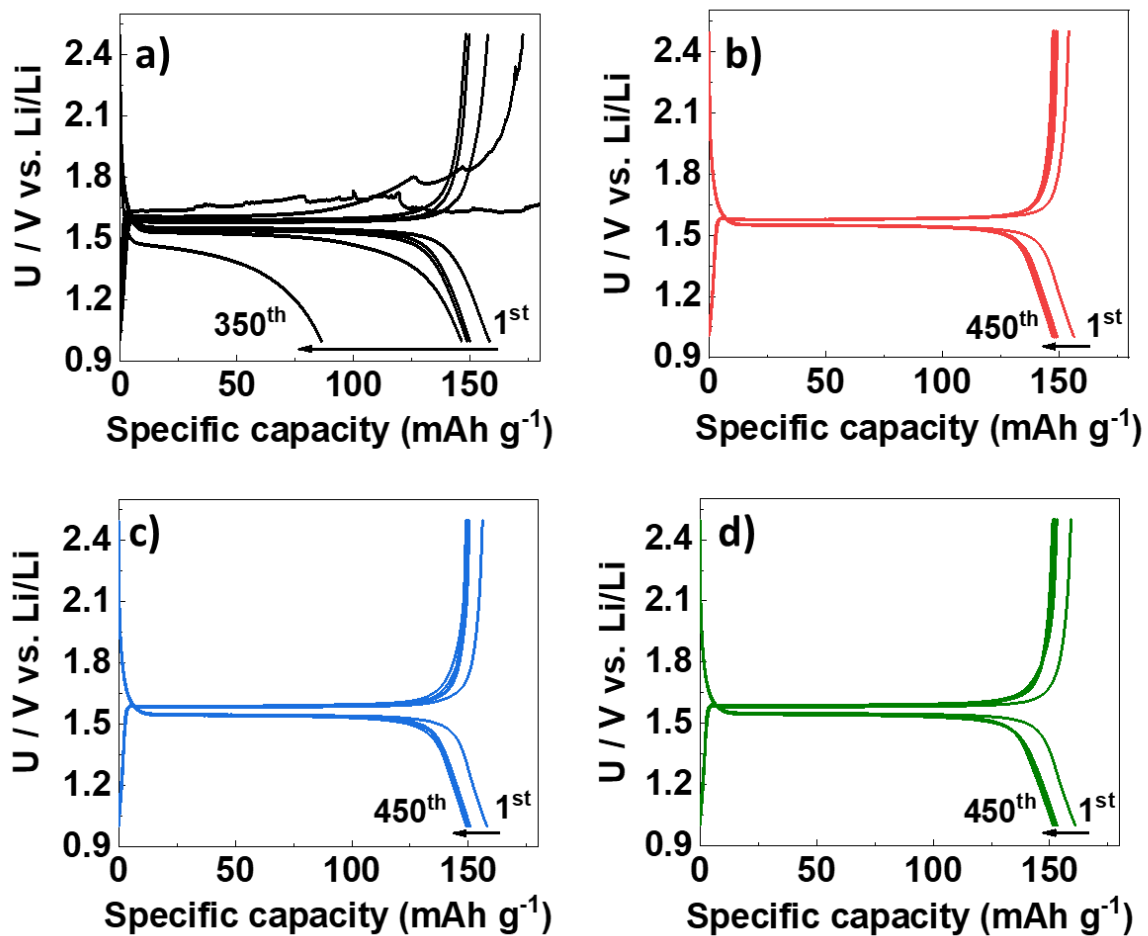


**Fig. S20.** Charge–discharge profiles of Li||LTO full cells cycled at 0.6 C using; (a) 1 M LiFSI in DME, (b) 1 M LiFSI in BTFE:DME, (c) 1 M LiFSI in BTFD:DME, and (d) 2 M LiFSI in BTFD:DME electrolytes.

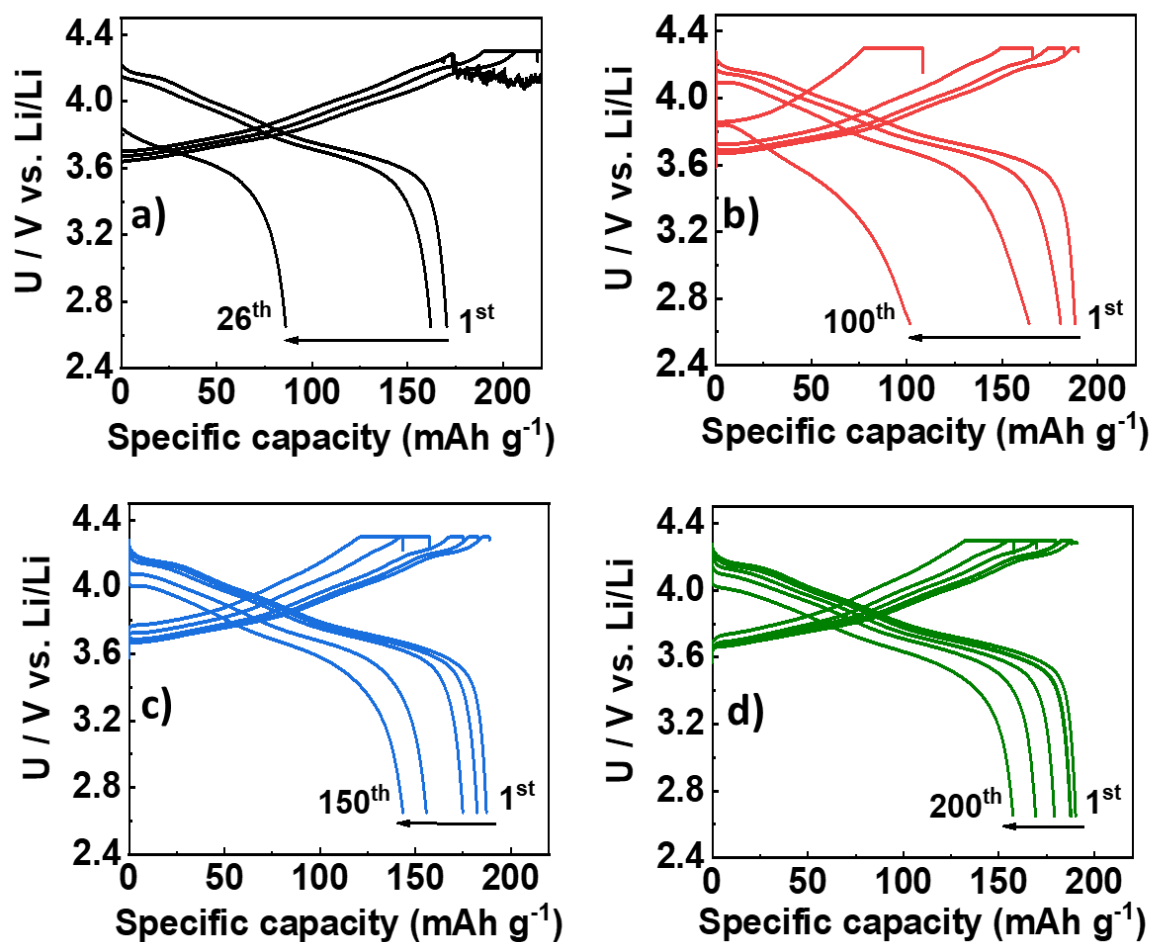


**Fig. S21.** Charge–discharge profiles of Li||NMC811 full cells cycled at 0.3 C using: (a) 1 M LiFSI in DME, (b) 1 M LiFSI in BTFE:DME, (c) 1 M LiFSI in BTFD:DME, and (d) 2 M LiFSI in BTFD:DME electrolytes.

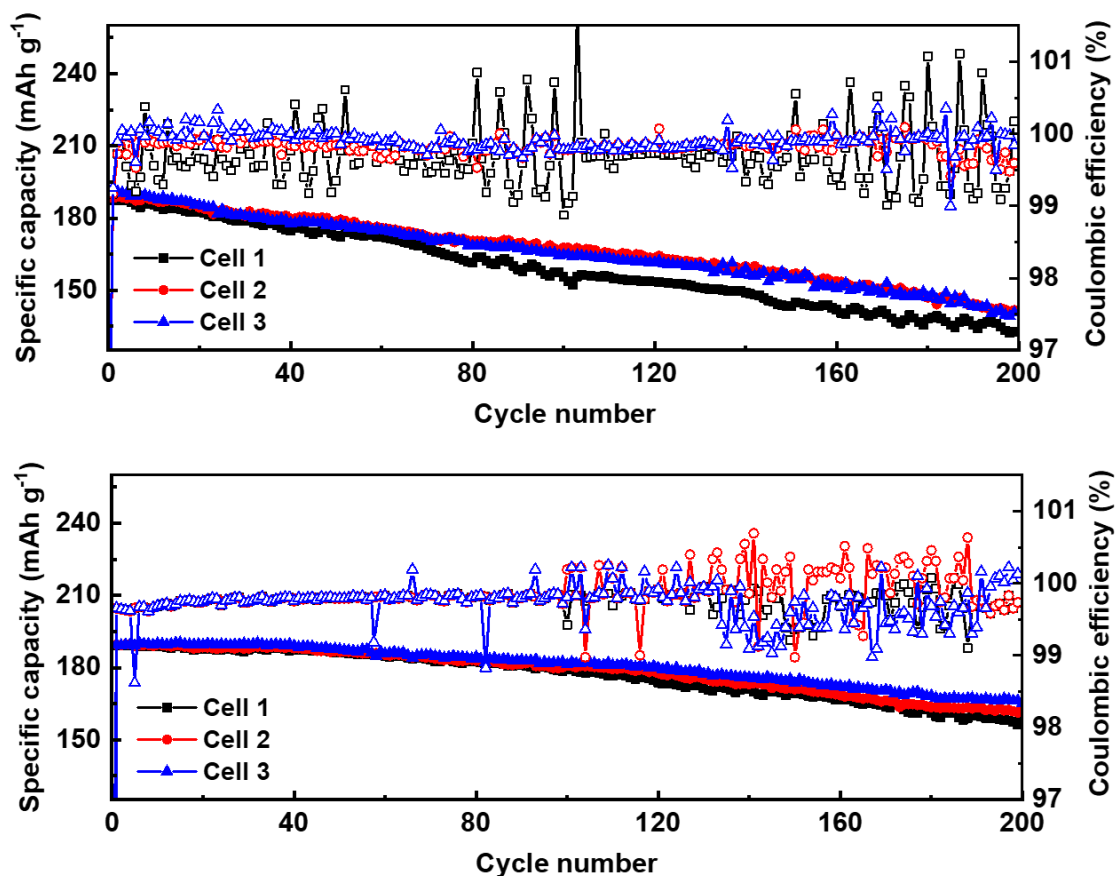


**Fig. S22.** Capacity and CE of Li | NMC811 full cells cycled at 0.3 C using: (a) 1 M LiFSI in BTFD:DME and (b) 2 M LiFSI in BTFE:DME electrolytes.

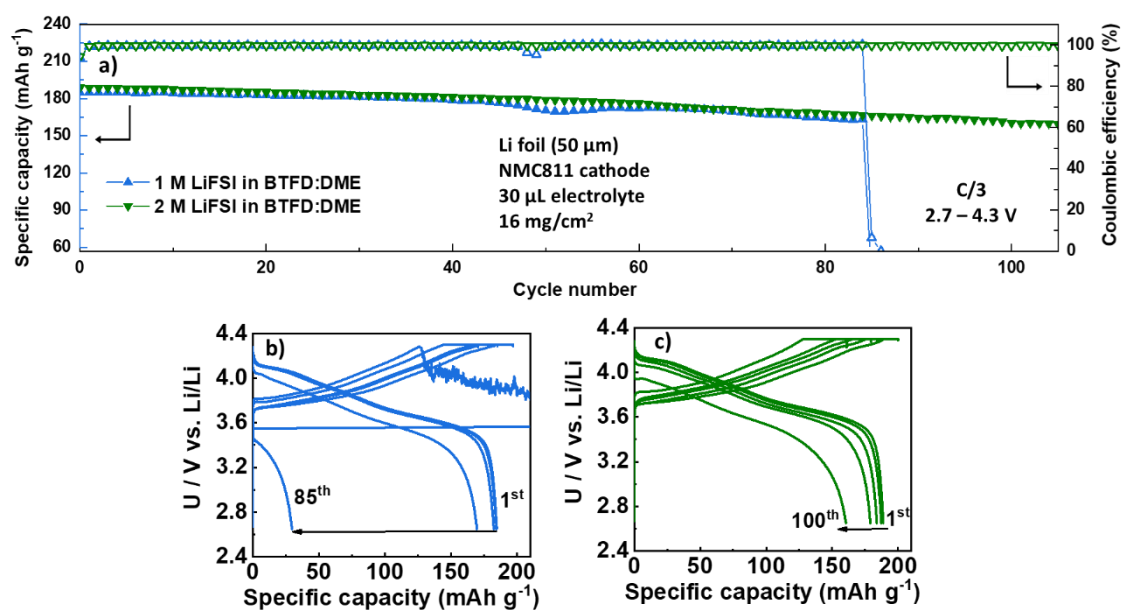


**Fig. S23.** (a) Electrochemical cycling performance comparison of Li | NMC811 full cells with a high loading NMC811 cathode (16 mg cm<sup>-2</sup>) paired with a thin Li metal anode foil (50  $\mu$ m). Charge-discharge

profiles of Li||NMC811 full cells cycled at 0.3 C using (b) 1 M LiFSI in BTFD:DME and (c) 2 M LiFSI BTFD:DME electrolytes.

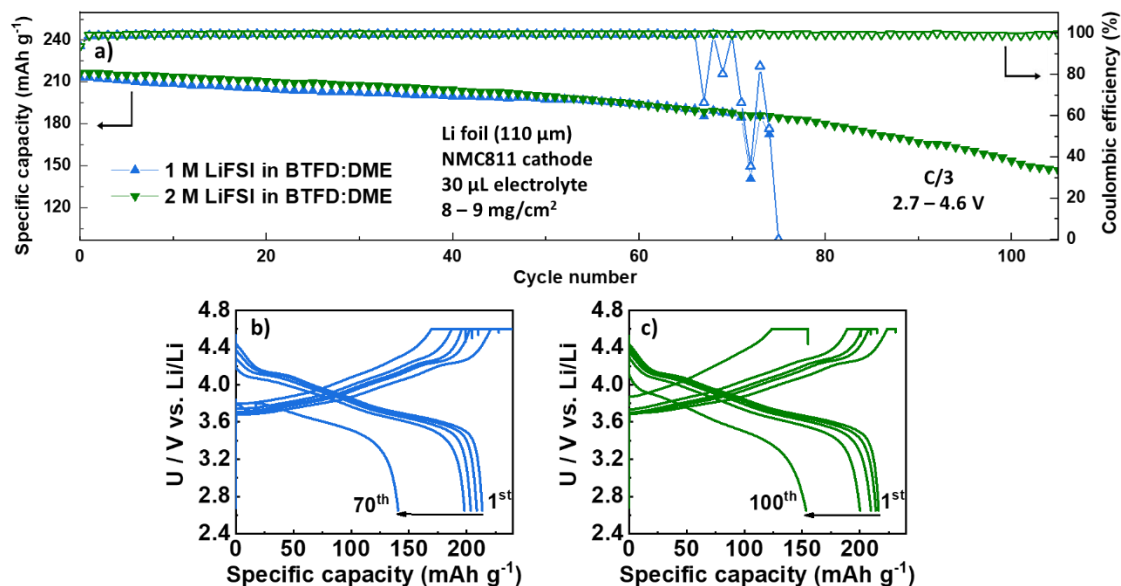


**Fig. S24.** (a) Electrochemical cycling performance comparison of Li||NMC811 full cells in the high-voltage range of 2.7 - 4.6 V. Charge-discharge profiles of Li||NMC811 full cells cycled at 0.3 C using (b) 1 M LiFSI in BTFD:DME and (c) 2 M LiFSI BTFD:DME electrolytes.

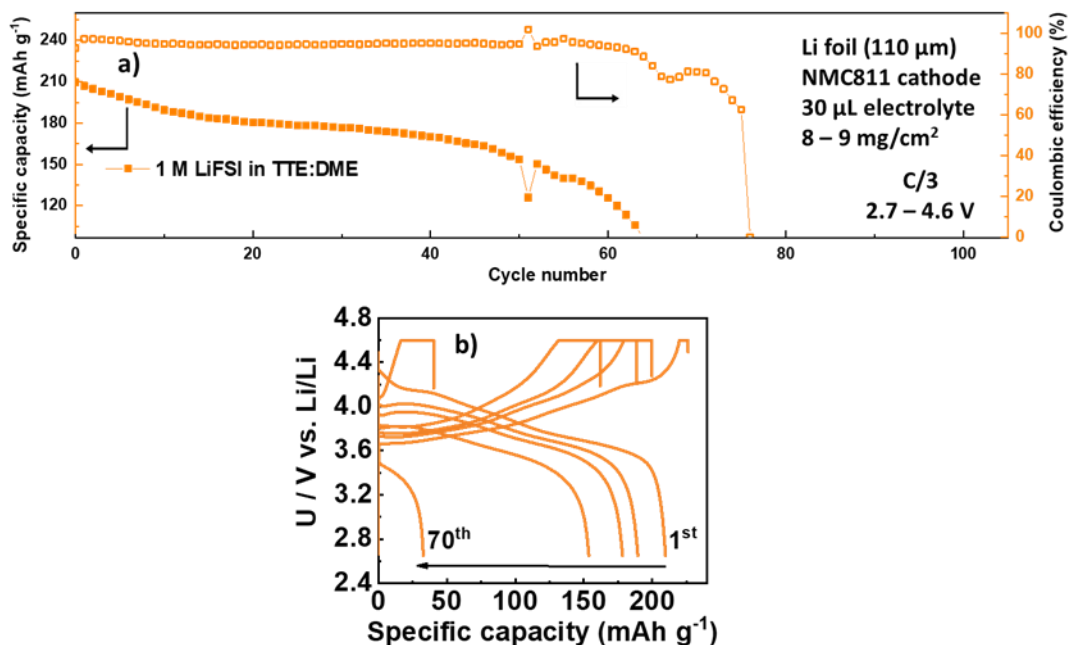


**Fig. S25.** (a) Electrochemical cycling performance comparison of Li||NMC811 full cells in the high-voltage range of 2.7 - 4.6 V with 1 M LiFSI TTE:DME electrolyte. Charge-discharge profiles of Li||NMC811 full cells cycled at 0.3 C using 1 M LiFSI TTE:DME electrolytes.

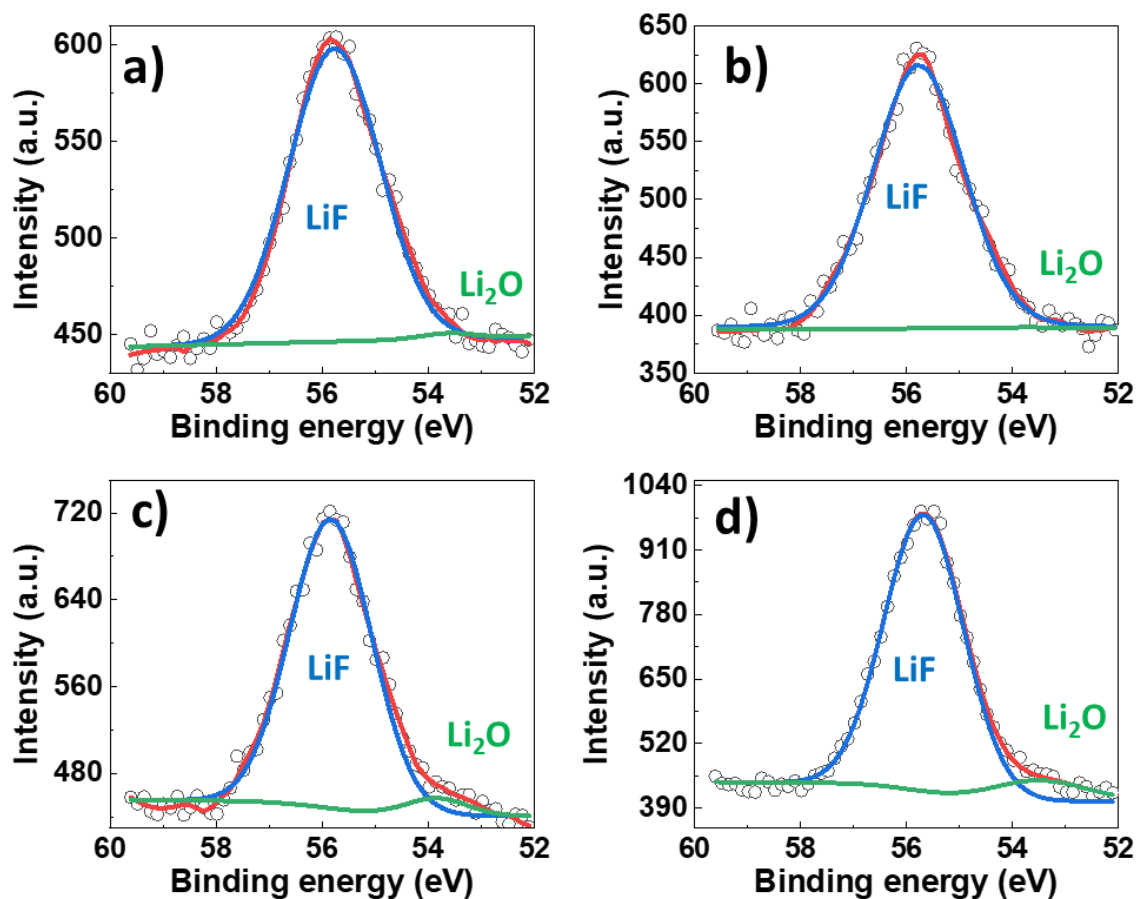


**Fig. S26.** Fitted Li 1s XPS spectra of NMC811 cathode cycled for 50 cycles at 0.3 C using: (a) 1 M LiFSI in DME, (b) 1 M LiFSI in BTFE:DME, (c) 1 M LiFSI in BTfD:DME, and (d) 2 M LiFSI in BTfD:DME electrolytes.

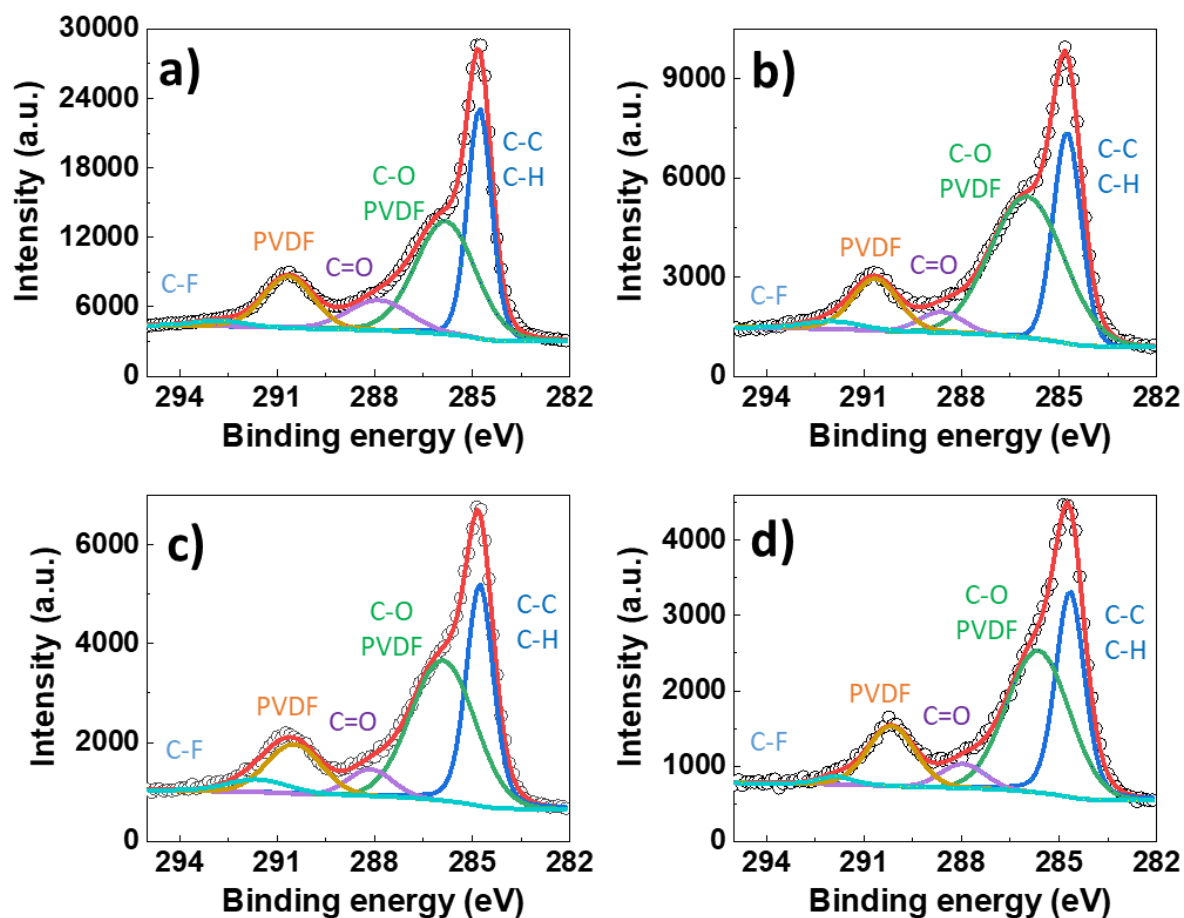


**Fig. S27.** Fitted C 1s XPS spectra of NMC811 cathode cycled for 50 cycles at 0.3 C using: (a) 1 M LiFSI in DME, (b) 1 M LiFSI in BTFE:DME, (c) 1 M LiFSI in BTFD:DME, and (d) 2 M LiFSI in BTFD:DME electrolytes.

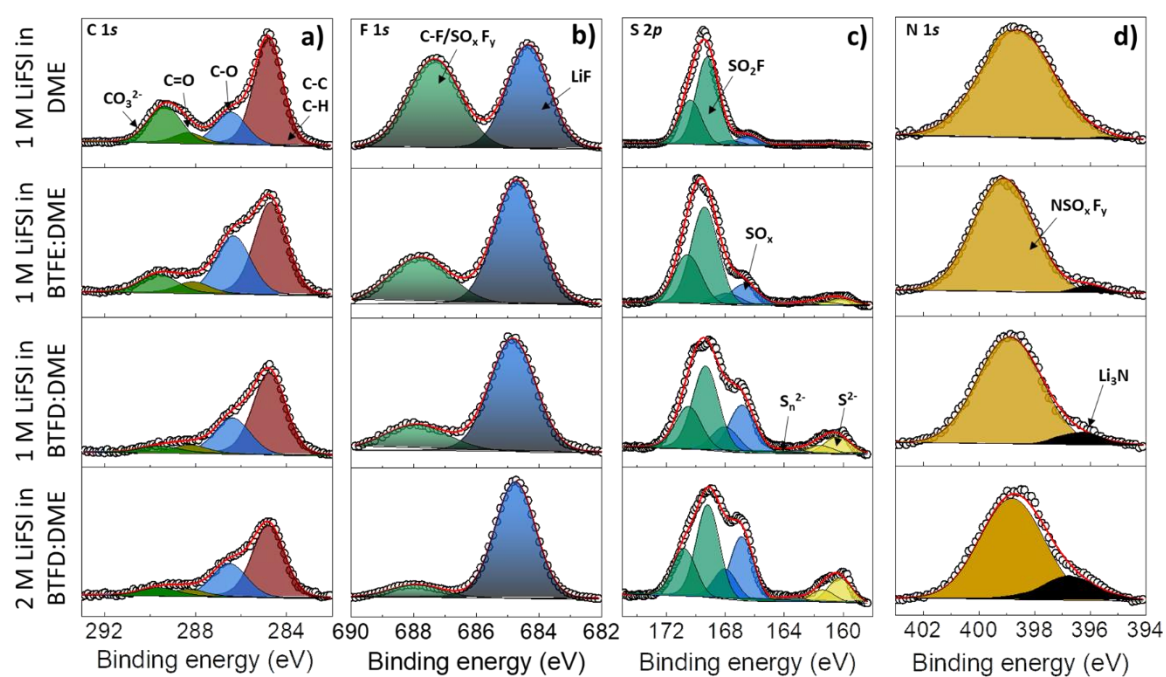


**Fig. S28.** Fitted XPS spectra measured on cycled Li anode extracted from Li || NMC811 cells for (a) C 1s, (b) F 1s, (c) S 2p, and (d) N 1s.

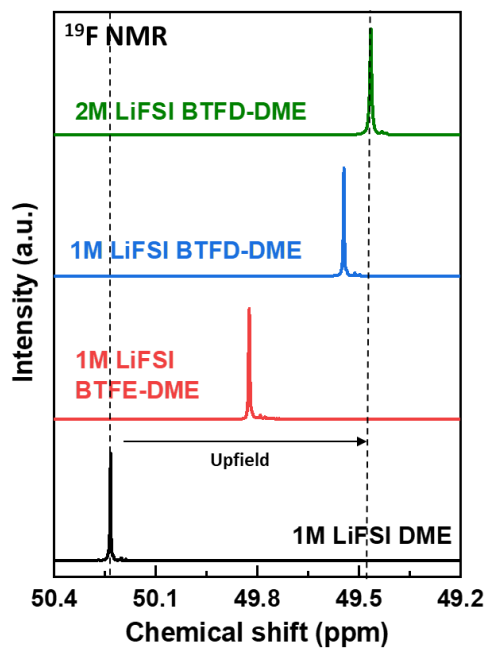


**Fig. S29.**  $^{19}\text{F}$  NMR spectra of different electrolytes.

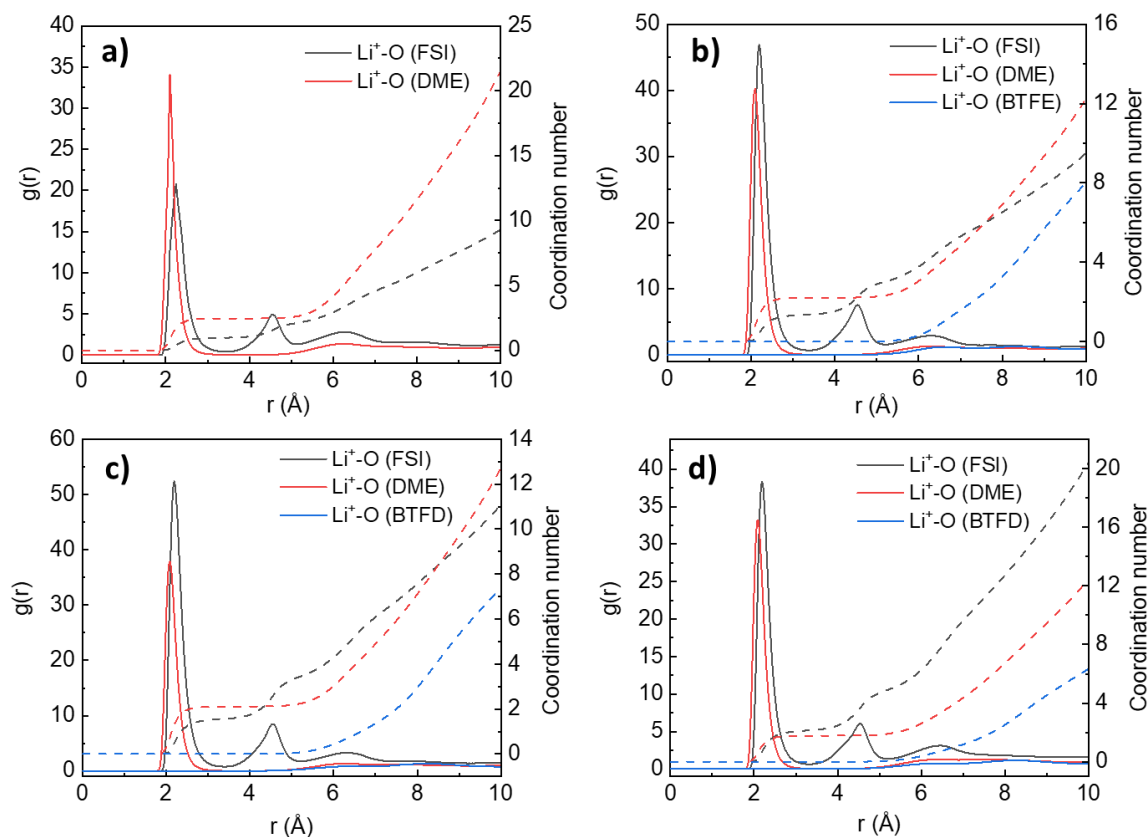


**Fig. S30.** Li<sup>+</sup>-O radial distribution functions from the MD simulation trajectories for: (a) 1 M LiFSI in DME, (b) 1 M in LiFSI in BTFE:DME, (c) 1 M LiFSI in BTFD:DME, and (d) 2 M LiFSI in BTFD:DME electrolytes.

For the local structure analysis, radial distribution functions (RDFs) depicting the relationship between lithium (Li<sup>+</sup>) and oxygen atoms within the solvent molecules were computed from the MD simulation trajectories (**Fig. S30**). The Li<sup>+</sup>-O (FSI) and Li<sup>+</sup>-O (DME) pair-wise interactions exhibit typical characteristics, with the RDFs revealing distinct and pronounced first peaks. As the distance increases, fluctuations in amplitude gradually diminish, converging towards unity at longer distances, indicating the short-range order and long-range disorder inherent in the liquid state. The first sharp peaks correspond to the first solvation shell, indicating that lithium primarily interacts with the oxygen atoms of the anion and the solvent DME. The Li<sup>+</sup>-O (BTFE) and Li<sup>+</sup>-O (BTFD) pair-wise interactions are virtually non-existent in the first solvation shells. To determine the coordination number (CN) within the first coordination shell of Li<sup>+</sup>, the radial distance is selected as the first minimum observed in the corresponding RDF. The cumulative CNs are depicted by dashed lines in **Fig. S30**.



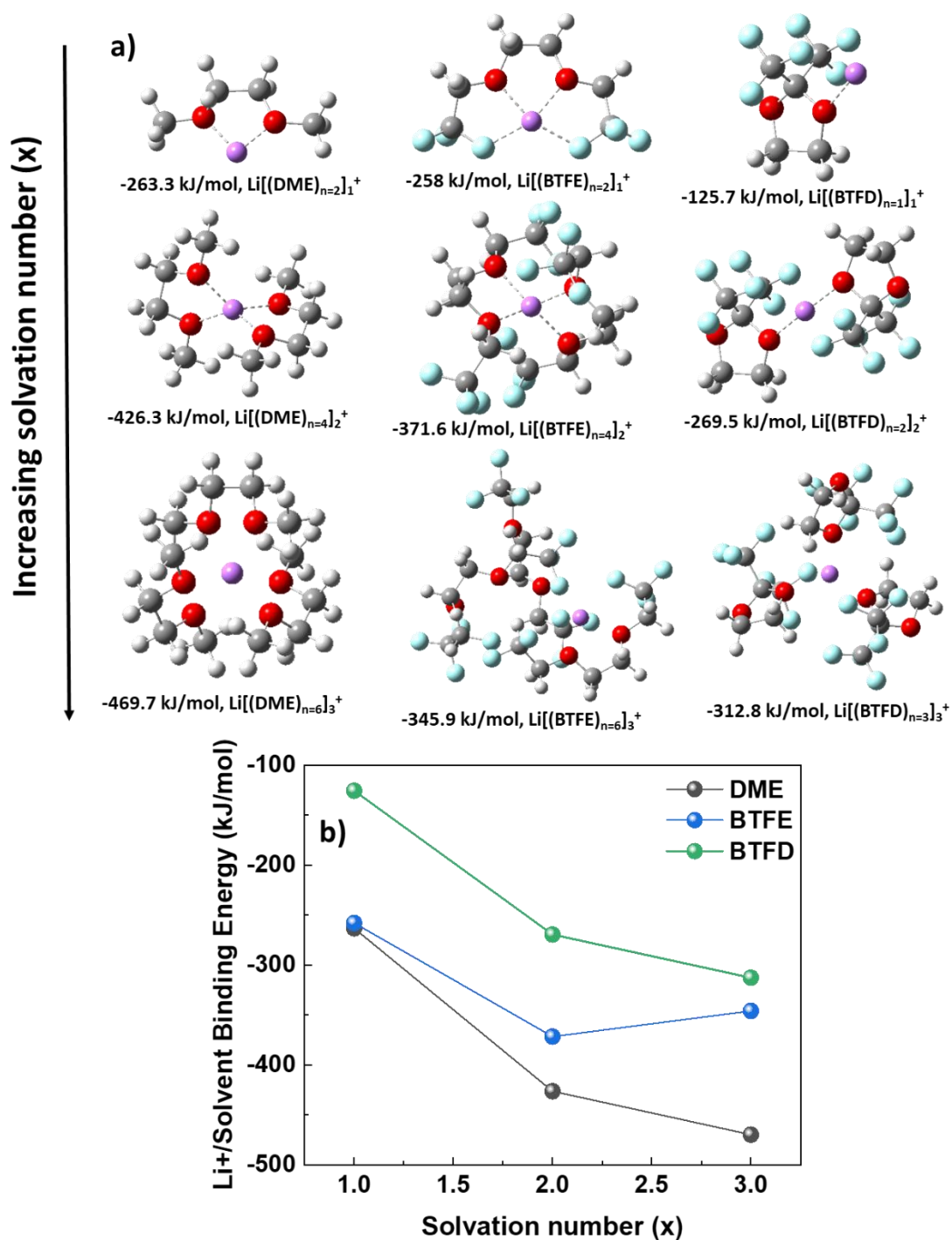


**Fig. S31.** (a) Optimized geometries and DFT calculated binding energies of  $\text{Li}[(\text{solvent})_n]_x^+$  complexes, where  $n$  is the  $\text{Li}^+$  CN and  $x$  is the  $\text{Li}^+$  SN. (b) Binding energy as function of SN ( $x$ ) for the different solvents.

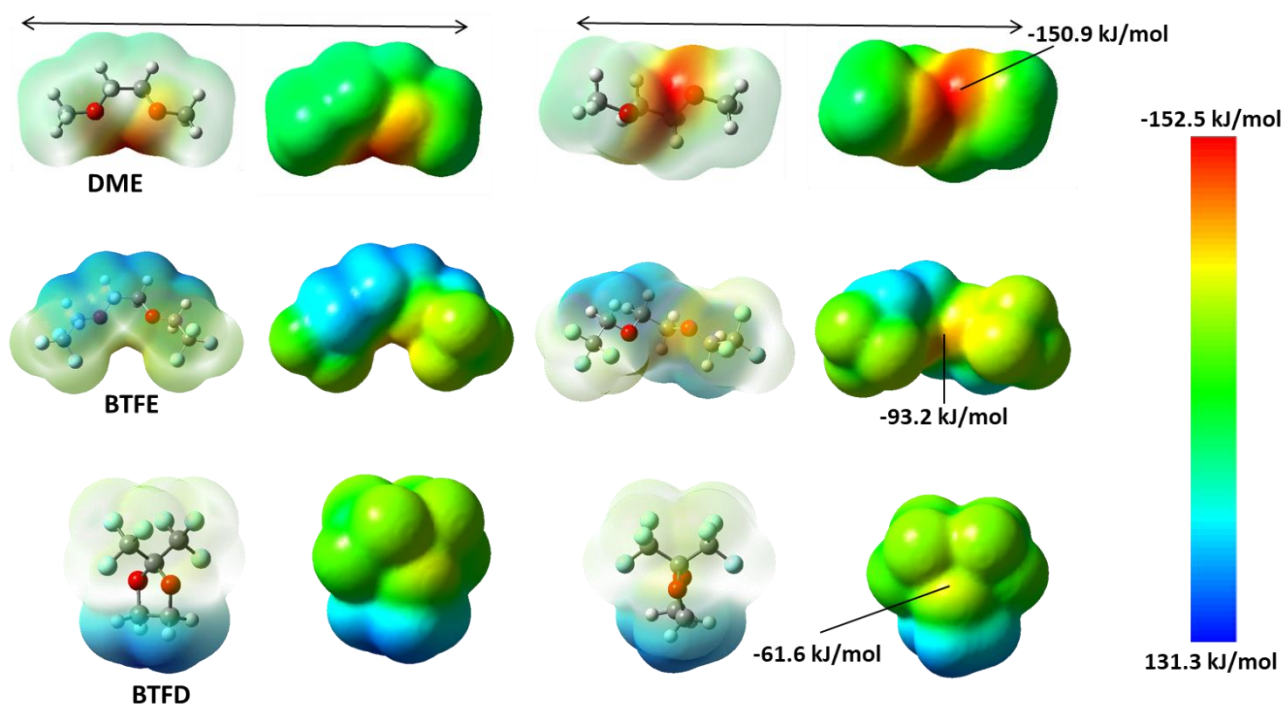


**Fig. S32.** ESPs calculated by DFT of the different solvents.

## REFERENCES

- [1] B.D. Adams, J. Zheng, X. Ren, W. Xu, J.G. Zhang, Accurate Determination of Coulombic Efficiency for Lithium Metal Anodes and Lithium Metal Batteries, *Adv. Energy Mater.* 8 (2018). <https://doi.org/10.1002/aenm.201702097>.
- [2] M.J. Frisch, G.W. Trucks, H.B. Schlegel, G.E. Scuseria, M.A. Robb, J.R. Cheeseman, G. Scalmani, V. Barone, B. Mennucci, G.A. Petersson, Gaussian 09, Revision A. 02; Gaussian, Inc., Wallingford CT, (2016).